

# Rigid Body Dynamics in Ambient Fluids

MARCEL PADILLA, ETH Zürich, Switzerland

AVIV SEGALL, ETH Zürich, Switzerland

OLGA SORKINE-HORNUNG, ETH Zürich, Switzerland

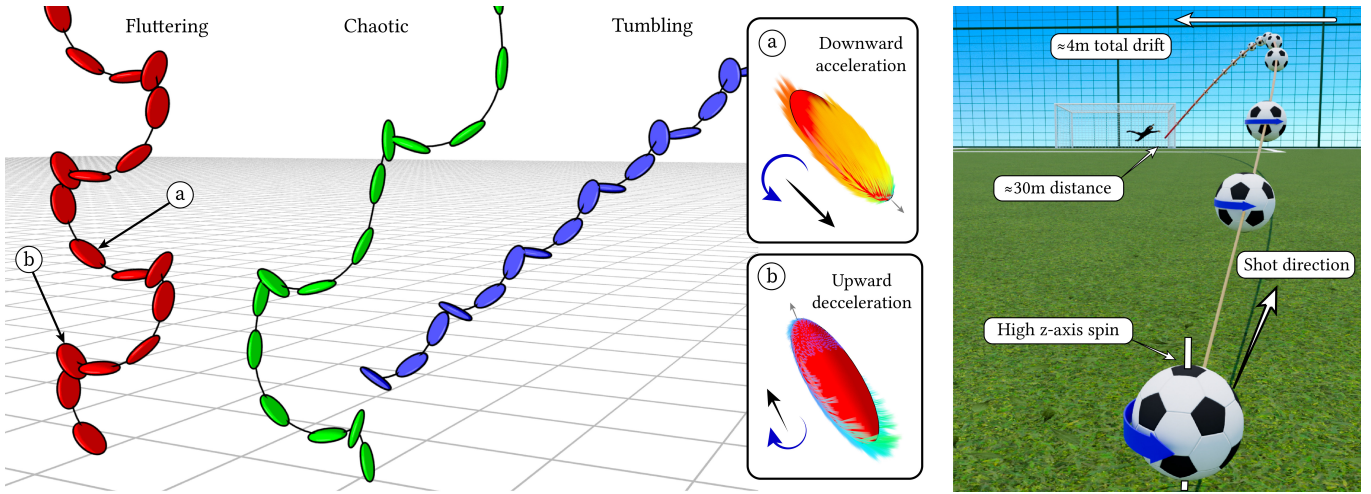


Fig. 1. Our extension to rigid body dynamics enables real-time simulation of fluid–body interactions without fluid solvers. We reproduce the unsteady behavior of falling plates (left) by estimating surface slip velocity and flow separation (center) to compute dynamic pressure forces. The model robustly captures phenomena such as the Magnus effect, enabling curved trajectories of spinning bodies (right) as well as many other phenomena.

We present a novel framework for rigid body dynamics in ambient media, such as air or water, enabling accurate motion prediction of objects without requiring computational fluid dynamics simulations. Our method computes the added mass of the fluid and replaces heuristic models for shape-dependent lift and drag with a generalized estimate of flow separation and dynamic pressure. Our method is the first within the rigid body dynamics context to reproduce the full range of falling plate behaviors: fluttering, tumbling, chaotic and steady modes, as well as phenomena such as the Magnus effect and the flight dynamics of an American football (tight spiral pass paradox). The resulting algorithm is simple to implement, robust, does not rely on specialized integrators and incorporates seamlessly into existing physics engines for real-time simulation.

CCS Concepts: • Computing methodologies → Physical simulation; Shape analysis; Real-time simulation.

Additional Key Words and Phrases: rigid body dynamics, added mass, potential flow, flow separation, real-time simulation

## 1 Introduction

Every object's motion is affected by its interaction with the *ambient fluid media*, such as air or water. However, accurately simulating the intricate dynamics of objects immersed in such fluids presents a formidable challenge in computer graphics, either requiring computationally expensive fluid simulations or relying on simplified heuristic models that struggle to capture complex physical phenomena. Such phenomena include thin falling plates, which exhibit unstable, chaotic motion due to their interaction with air (Fig. 1).

Authors' Contact Information: Marcel Padilla, ETH Zürich, Switzerland; Aviv Segall, ETH Zürich, Switzerland; Olga Sorkine-Hornung, ETH Zürich, Switzerland.

Traditional rigid body dynamics (RBD) frameworks effectively model motion in a vacuum and have been a fundamental contribution to the landscape of fast physical simulation, becoming the scalable and go-to method for the physical motion of rigid objects in modern animation software. The realism of the simulation results relies on the object's momentum being large enough for the effects of the ambient fluid to remain negligible, which is often not the case for light, small or fast-moving objects. Accurately representing the subtle interplay between an object and its surrounding medium, including effects such as anisotropic fluid inertia, coupled linear and angular motion, lift, drag and friction requires a more robust approach than conventional approximations, which current tools do not provide [Soliman et al. 2024; Weißmann and Pinkall 2012b].

When fluid–body interactions cannot be neglected, the standard approach is to represent and simulate the surrounding fluid, incurring significant computational cost, or to adopt simplified models that approximate drag and lift forces using heuristic or data-driven coefficients (see Sec. 2).

In this paper we present a novel framework for rigid body dynamics in incompressible ambient fluids such as air or water that enables more accurate simulations of bodies moving through fluid media without requiring volumetric fluid solvers. Our focus is on flows where large-scale turbulence is not dominant including still or gently varying conditions. We show that in this regime, a careful treatment of added mass, flow separation and surface pressure forces suffices to reproduce a broad spectrum of complex fluid–body interaction phenomena. Our core contributions include:

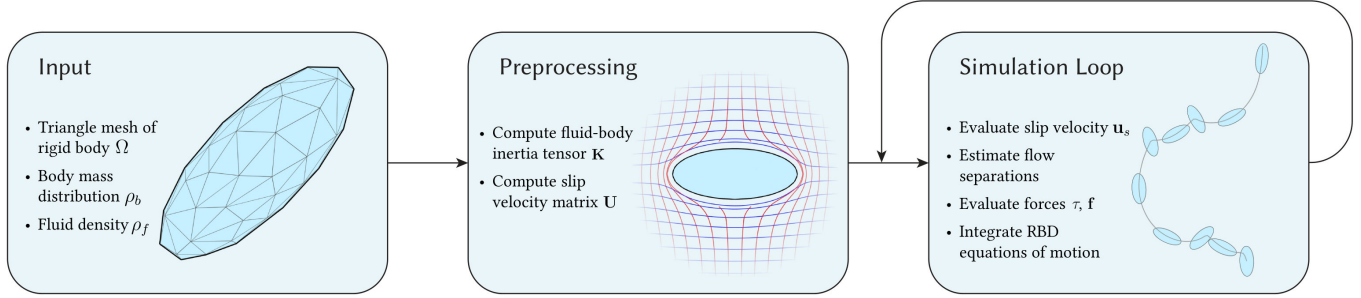


Fig. 2. Overview of our algorithm. Given a watertight triangulated surface mesh and physical parameters as input, we first perform preprocessing to compute quantities invariant during runtime. In the simulation loop, our proposed forces are computed and then integrated in the standard rigid-body dynamics way.

- (1) **An improved fluid force model based on surface slip velocity and flow separation estimation**, allowing the computation of dynamic pressure forces without relying on heuristic lift or drag coefficients and non-physical parameters.
- (2) **A simple and physically grounded algorithm for fluid–body interaction**, capable of producing complex motion phenomena in real time and dependent on only one physically plausible parameter. The method requires only augmenting the  $6 \times 6$  inertia tensor and the application of additional forces, enabling seamless integration into standard rigid body solvers without changes to their infrastructure (Fig. 2).
- (3) **Accurate reproduction of complex fluid–body interaction phenomena** such as fluttering, tumbling and chaotic descent, the Magnus effect, golf ball trajectories, the flight dynamics of an American football, underwater motion, buoyant motion and spinning toys.

Our approach aims to advance the modeling of fluid–body interactions and improve the efficiency vs. fidelity trade-off. The results provide a robust upgrade to rigid body dynamics in incompressible, non-turbulent media and is applicable across a wide range of simulation scenarios.

## 2 Related work

The foundational equations governing the motion of rigid bodies, first formulated by Euler in the 18th century, remain central to modern mechanics [Goldstein et al. 2002; Landau and Lifshitz 1976] and form the basis for many physically-based animation techniques. A widely used introduction can be found in the course notes by Baraff [1997].

**Body–fluid interaction.** A wide range of previous work tackle fluid–solid coupling by explicitly simulating fluid media such as air and water. The foundational techniques for this include particle-based methods [Carlson et al. 2004], direct-forcing schemes [Becker et al. 2009], smoothed particle hydrodynamics formulations [Akinci et al. 2012] and reduced-order models [Treuille et al. 2006]. The reliance on full fluid simulation continues in state-of-the-art research for tasks such as control, frictional contact, stability and aerodynamic design [Banks et al. 2017; Le et al. 2024; Li et al. 2023; Probst and

Teschner 2023; Roenby et al. 2024]. In contrast to these approaches, our method does not require computationally expensive fluid volume simulations. Instead, it predicts the influence of the fluid on the rigid body directly via geometric arguments using only the surface of the object.

*Motion in fluids without fluid simulations.* A growing body of research shows that complex fluid behaviors can be captured without full volumetric fluid solvers by leveraging physics-informed models. For example, Ozgen et al. [2010] simulate cloth dynamics using fractional derivatives that capture drag forces directly, while Lannes [2017] formulates the dynamics of floating solids purely in terms of surface pressures. Vortex-based approaches offer another compelling example: several works demonstrate the ability to reproduce smoke, vortex rings and related effects using filament primitives instead of fluid solvers [Angelidis and Neyret 2005; Padilla et al. 2019; Weißmann and Pinkall 2010a]. Gross et al. [2023] achieve swimmer-like motions through purely shape-driven dissipation, and Soliman et al. [2024] replicate motion-in-fluid phenomena using simplified and a fast local added mass estimator on convex surfaces. Weißmann and Pinkall [2012b] introduce Kirchhoff tensor-based added mass into rigid body dynamics and can be seen as the direct predecessor of our work, as further discussed in Sec. 4. Together, these methods demonstrate that bulk fluid representation and simulation are often unnecessary to model compelling fluid effects, a principle that motivates this work.

*Simplified fluid response models.* A common strategy for approximating fluid forces in real time is the use of simplified aerodynamic models based on drag- and lift coefficients. This approach has a long history in animation [Wejchert and Haumann 1991] and remains prevalent across diverse applications, including the simulation of bird flight [Wu and Popović 2003], artificial fishes [Tu and Terzopoulos 1994], insect flight [Chen et al. 2024] and soft-bodied animals [Min et al. 2019], as well as in tools for designing gliders [Umetani et al. 2014] and modeling general fluid–body phenomena [Soliman et al. 2024]. While computationally efficient, these approaches rely on empirically derived or tuned coefficients that are shape-specific, dependent on angle of attack, and therefore do not yield good results for arbitrary input shapes. In contrast, our method computes fluid responses for arbitrary geometries while resorting to a single physical parameter, the flow separation angle.

Table 1. Summary of frequently used symbols.

Symbol	Description
$B$	Simply connected domain of the rigid body in $\mathbb{R}^3$
$\Omega$	Exterior domain $\mathbb{R}^3 \setminus B$
$S$	Boundary of the rigid body (surface) $\partial B$
$z$	Position vector in $\mathbb{R}^3$
$n$	Outward unit normal to the body surface
$w$	Rigid body angular velocity in body frame, 1/s.
$v$	Rigid body linear velocity in body frame, m/s
$l$	Rigid body angular momentum in body frame, kg m <sup>2</sup> /s
$p$	Rigid body linear momentum in body frame, kg m/s
$\rho_f$	Fluid density, kg/m <sup>3</sup>
$\alpha$	Flow separation angle, rad
$K_b$	Body $6 \times 6$ inertia tensor
$K_f$	Fluid $6 \times 6$ inertia tensor
$K$	Combined inertia tensor
$\phi$	Fluid velocity potential in $\Omega$
$(\cdot)^\parallel$	Tangential component to the normal $n$
$(\cdot)^\perp$	Normal component on the surface.
$u$	Fluid velocity field in $\Omega$ , m/s
$u_s^\phi$	Potential surface slip velocity, m/s
$u_s$	Surface slip velocity, m/s
$f_{dp}$	Dynamic pressure force, N
$P_\phi$	Potential $\#V \times 6$ matrix
$U$	Slip velocity $3\#F \times 6$ matrix

*Falling modes of thin plates.* The simulation of freely falling plates that exhibit fluttering, tumbling or chaotic motion remains an active and challenging research area dating back to Newton [1687] and Maxwell [1890]. Numerous studies have addressed this phenomenon using full fluid simulations, often relying on Navier–Stokes solvers or immersed boundary methods to model vortex shedding and dynamic mode transitions [Andersen et al. 2005; Pesavento and Wang 2004; Rana et al. 2020; Wu and Lin 2015]. Experimental investigations have guided these results, highlighting the sensitivity of falling behavior to moments of inertia, vortex interactions and initial conditions [Huang et al. 2013; Xiang et al. 2018; Zhong et al. 2011]. Although simplified or inviscid approaches [Sohn 2024] have been explored, they still rely on specialized fluid solvers or remain limited in generality (only ellipses).

In contrast to the above approaches, our method introduces a general, simulation-free, surface-based formulation that, for the first time, reproduces the full spectrum of falling thin plates and other intricate phenomena, without requiring volumetric fluid simulation or heuristic drag- and lift coefficients. In doing so, we narrow the long-standing gap between real-time fluid-body interaction methods and the ability to recreate complex ambient fluid interactions.

### 3 Background

We briefly recall the foundational equations of rigid body dynamics (RBD), which we subsequently extend to incorporate fluid interactions in Sec. 4. In Table 1 we provide an overview of the symbols used through this work.

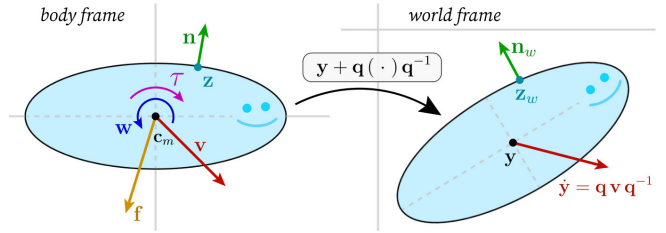


Fig. 3. State variables of a rigid body dynamics system. In the body frame (left), angular velocity  $w$  and linear velocity  $v$  define the motion, along with applied torque  $\tau$  and force  $f$ . The world frame (right) tracks the body’s position  $y$  and orientation  $q \in \mathbb{S}^3$ . Frame transformations are performed via quaternion conjugation, e.g.,  $\dot{y} = q v q^{-1}$ .

### 3.1 Rigid body dynamics

We model a rigid body as a simply connected domain  $B \subset \mathbb{R}^3$  enclosed by a watertight surface  $S = \partial B$  with outward pointing normals  $n \in \mathbb{S}^2$ . The state is described by the position  $y \in \mathbb{R}^3$  and orientation  $q \in \mathbb{S}^3$  (a unit quaternion), both expressed in world coordinates. The angular and linear velocities  $w, v \in \mathbb{R}^3$  are defined in a body-fixed frame placed at the center of mass  $c_m$  (Fig. 3). The corresponding angular and linear momenta  $l, p \in \mathbb{R}^3$  are related to the velocities by a symmetric positive definite inertia tensor  $K \in \mathbb{R}^{6 \times 6}$ :

$$\begin{bmatrix} l \\ p \end{bmatrix} = K \begin{bmatrix} w \\ v \end{bmatrix}. \quad (1)$$

In classical RBD, which assumes a vacuum in the ambient space,  $K$  is given by the *body inertia tensor*

$$K_b = \begin{bmatrix} J & 0 \\ 0 & m \text{Id} \end{bmatrix}, \quad (2)$$

where  $J \in \mathbb{R}^{3 \times 3}$  is the body’s rotational inertia,  $m$  is its mass, and  $\text{Id}$  is the identity matrix. Notice how  $K_b$ ’s block diagonal structure decouples the angular and linear components. A position  $z \in S$  in the body-fixed frame is transformed to the world frame via  $z_w = y + q z q^{-1}$ , where  $z$  is interpreted as a pure quaternion (zero scalar part). Directional quantities such as normals or forces are transformed by rotation only; the translation term  $y$  does not apply.

### 3.2 Equations of motion

The RBD differential equations are given by

$$\dot{y} = q v q^{-1}, \quad \dot{q} = \frac{1}{2} q w, \quad (3)$$

$$\begin{bmatrix} \dot{l} \\ \dot{p} \end{bmatrix} = \underbrace{\begin{bmatrix} l \times w + p \times v \\ p \times w \end{bmatrix}}_{(\tau_{gyro}, f_{gyro})^\top :=} + \begin{bmatrix} \tau \\ f \end{bmatrix}. \quad (4)$$

The gyroscopic terms in  $(\tau_{gyro}, f_{gyro})$  arise because the dynamics are expressed in a non-inertial (rotating) body frame (see [Weißmann and Pinkall 2012b] for a derivation). The external torque  $\tau$  and force  $f$  in the body frame may include contributions from gravity, buoyancy or fluid interactions. Equation (1) is used to convert the momenta  $(l, p)$  back into the angular and linear velocities  $(w, v)$ .

## 4 Fluid interactions

We consider the motion of a rigid body immersed in a quiescent (i.e. still), incompressible fluid domain  $\Omega = \mathbb{R}^3 \setminus B$  with constant density  $\rho_f$ . The fluid influences the body's dynamics primarily through two mechanisms: the transfer of momentum and the dynamic pressure along the body's surface. We first review the potential flow (Sec. 4.1) and its resulting added mass (Sec. 4.2) as seen in [Weißmann and Pinkall 2012b] before introducing our core contribution of pressure analysis (Sec. 4.3) with flow separation (Sec. 4.4).

### 4.1 Potential flow

In the body-fixed frame, each point  $\mathbf{z} \in S$  of the surface moves with the rigid body velocity  $\dot{\mathbf{z}} = \mathbf{v} + \mathbf{w} \times \mathbf{z}$ . This motion induces a velocity field  $\mathbf{u}$  in the surrounding fluid, constrained by the no-penetration condition  $\langle \mathbf{n}, \mathbf{u} \rangle = \langle \mathbf{n}, \dot{\mathbf{z}} \rangle$  on the surface. The associated kinetic energy of the fluid is given by

$$E_{\text{kin}} = \int_{\Omega} \rho_f \|\mathbf{u}\|^2 dV = \rho_f \int_{\Omega} \|\mathbf{u}\|^2 dV. \quad (5)$$

Given  $\mathbf{v}$  and  $\mathbf{w}$ , the velocity field  $\mathbf{u}$  that minimizes the fluid kinetic energy  $E_{\text{kin}}$  is the gradient of a harmonic *potential* field  $\phi : \Omega \rightarrow \mathbb{R}$ . This field satisfies the following Neumann boundary value problem:

$$\begin{aligned} \partial_{\mathbf{n}_z} \phi(\mathbf{z}) &= \langle \mathbf{n}(\mathbf{z}), \mathbf{v} + \mathbf{w} \times \mathbf{z} \rangle, \quad \text{for } \mathbf{z} \in S, \\ \Delta \phi(\mathbf{z}) &= 0, \quad \text{for } \mathbf{z} \in \Omega, \\ \phi(\mathbf{z}) &\rightarrow 0, \quad \text{as } \|\mathbf{z}\| \rightarrow \infty. \end{aligned} \quad (6)$$

The resulting velocity field  $\mathbf{u} = \nabla \phi$  represents the incompressible, irrotational flow induced by the rigid body's motion through the fluid. Since the governing Laplace equation and the Neumann boundary condition in Eq. (6) are both linear in the velocity components  $\mathbf{w}, \mathbf{v}$ , the corresponding solution  $\phi$  depends linearly on these inputs. It follows that the general solution can be constructed as a linear superposition of six basis potentials, each corresponding to unit motion in one of the six canonical degrees of freedom (Fig. 4):

$$\begin{aligned} \phi &= \mathbf{w}_x \phi_{\mathbf{w}_x} + \mathbf{w}_y \phi_{\mathbf{w}_y} + \mathbf{w}_z \phi_{\mathbf{w}_z} + \mathbf{v}_x \phi_{\mathbf{v}_x} + \mathbf{v}_y \phi_{\mathbf{v}_y} + \mathbf{v}_z \phi_{\mathbf{v}_z} \\ &= \underbrace{[\phi_{\mathbf{w}_x} \ \phi_{\mathbf{w}_y} \ \phi_{\mathbf{w}_z} \ \phi_{\mathbf{v}_x} \ \phi_{\mathbf{v}_y} \ \phi_{\mathbf{v}_z}]}_{\mathbf{P}_\phi :=} (\mathbf{w}_x, \mathbf{w}_y, \mathbf{w}_z, \mathbf{v}_x, \mathbf{v}_y, \mathbf{v}_z)^\top \\ &= \mathbf{P}_\phi(\mathbf{w}, \mathbf{v})^\top. \end{aligned} \quad (7)$$

We denote this linear mapping from  $(\mathbf{w}, \mathbf{v})$  to the potential field  $\phi$  solution of Eq. (6) by  $\mathbf{P}_\phi$ .

### 4.2 Added mass

The angular and linear momentum imparted to the fluid by the body's motion can be computed explicitly using the divergence theorem (and using  $\phi(\mathbf{z}) \rightarrow 0$  for large  $\|\mathbf{z}\|$ ):

$$\begin{aligned} \mathbf{l}_f &= \int_{\Omega} \rho_f \mathbf{z} \times \nabla \phi(\mathbf{z}) dV_z = \rho_f \int_S \phi(\mathbf{z}) \mathbf{z} \times \mathbf{n} dA_z, \\ \mathbf{p}_f &= \int_{\Omega} \rho_f \nabla \phi(\mathbf{z}) dV_z = \rho_f \int_S \phi(\mathbf{z}) \mathbf{n} dA_z. \end{aligned} \quad (8)$$

These expressions are linear in  $\phi$ , and we denote the resulting linear operator  $\phi \mapsto (\mathbf{l}_f, \mathbf{p}_f)$  as  $\mathbf{M}_\phi$ . Composing this with the linear map  $\mathbf{P}_\phi : (\mathbf{w}, \mathbf{v}) \mapsto \phi$  from Sec. 4.1 yields

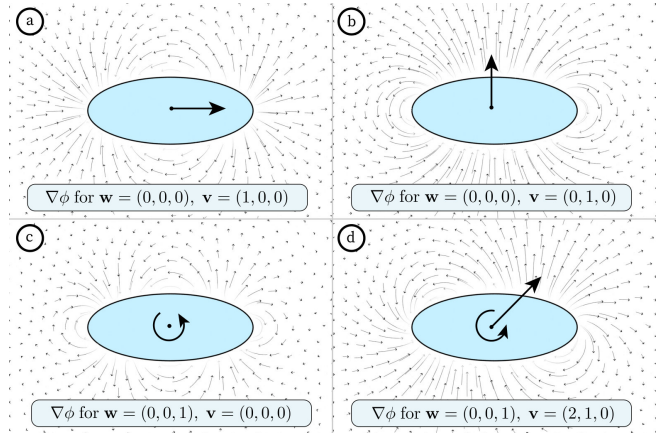


Fig. 4. Potential flow fields  $\mathbf{u} = \nabla \phi$  induced by different components of rigid body motion  $(\mathbf{w}, \mathbf{v})$  for an elliptical body (2D-slice view). (a) Horizontal translation induces weak fluid inertia. (b) Vertical translation yields a stronger inertial response. (c) Rotation around the center generates a distinct flow field. (d) General motion results from a linear combination of the six fundamental modes that correspond to the six degrees of freedom of motion (Eq. (7)).

$$\begin{bmatrix} \mathbf{l}_f \\ \mathbf{p}_f \end{bmatrix} = \mathbf{M}_\phi \phi = \underbrace{\mathbf{M}_\phi}_{\mathbf{K}_f :=} \mathbf{P}_\phi \begin{bmatrix} \mathbf{w} \\ \mathbf{v} \end{bmatrix}. \quad (9)$$

We refer to  $\mathbf{K}_f$  as the *fluid inertia tensor*. Following the classical formulation by Kirchhoff [1870], we augment the rigid body's inertia tensor to account for the influence of the surrounding fluid:

$$\mathbf{K} = \mathbf{K}_b + \mathbf{K}_f. \quad (10)$$

This additional contribution is known as the *added mass* effect, capturing the fluid's anisotropic resistance to acceleration (Fig. 4). The resulting total inertia tensor  $\mathbf{K}$  couples the rigid body and fluid inertia into a single unified system. Unlike the decoupled block-diagonal structure of  $\mathbf{K}_b$  in Eq. (1), the full tensor  $\mathbf{K}$  generally includes off-diagonal terms that link angular and linear momentum.

### 4.3 Surface flow and pressure

We now analyze the pressure induced by the flow onto the rigid body, which clearly distinguishes our method from previous work. In the world frame, the rigid body moves with velocity  $(\mathbf{v}, \mathbf{w})$  through a fluid, displacing it via the potential flow  $\nabla \phi$  subject to the Neumann boundary conditions on the surface  $S$ . In the body frame, this appears as a tangential flow along the surface, which we define as the *potential surface slip velocity*  $\mathbf{u}_s^\phi(\mathbf{z})$  at each point  $\mathbf{z} \in S$  (Fig. 5):

$$\mathbf{u}_s^\phi(\mathbf{z}) := \nabla \phi(\mathbf{z}) - (\mathbf{v} + \mathbf{w} \times \mathbf{z}). \quad (11)$$

Bernoulli's principle states that the pressure  $p$  of a fluid is given by

$$p(\mathbf{z}) = \underbrace{-\frac{1}{2} \rho_f \|\mathbf{u}_s^\phi(\mathbf{z})\|^2}_{\text{dynamic pressure } p_{\text{dyn}}} + \underbrace{-\rho_f \langle \mathbf{z}, \mathbf{g} \rangle}_{\text{hydrostatic pressure } p_{\text{hyd}}} + \underbrace{c}_{\text{const.}} \quad (12)$$

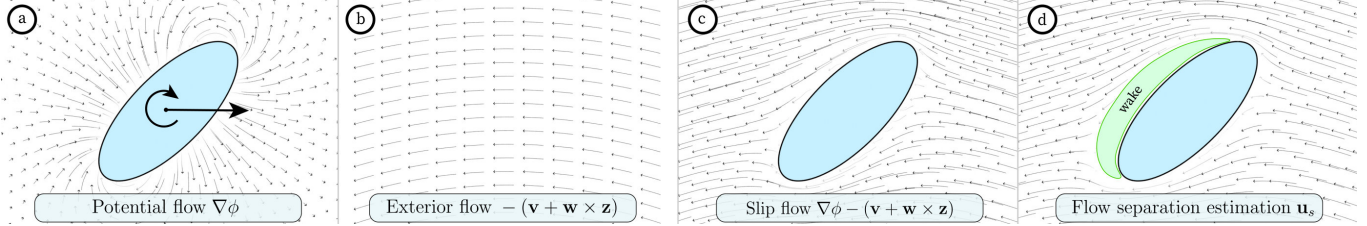


Fig. 5. Illustration of the relative flow around a rigid body. (a) Potential flow  $\nabla\phi$  induced in the world frame by the body's motion. (b) Rigid body velocity field in the opposite direction, shown in the body frame. (c) Superposition of (a) and (b) yields the flow past the body in the body frame. (d) We assume a small wake region where the surface slip velocity  $\mathbf{u}_s$  effectively vanishes.

where  $\mathbf{g} \in \mathbb{R}^3$  is the gravity vector in the body-frame. The pressure exerts a force in the local normal direction  $\mathbf{n}_z$ , resulting in the net pressure force on the rigid body

$$\mathbf{f}_p := \int_S p(\mathbf{z}) \mathbf{n}_z \, dA_z = \underbrace{\int_S p_{dyn} \mathbf{n}_z \, dA_z}_{\mathbf{f}_{dp} :=} + \underbrace{\int_S p_{hyd} \mathbf{n}_z \, dA_z}_{\mathbf{f}_{buo} :=} + \underbrace{\int_S c \mathbf{n}_z \, dA_z}_{\mathbf{f}_{const} :=}. \quad (13)$$

Using the divergence theorem, the hydrostatic pressure integrates to the familiar buoyant force  $\mathbf{f}_{buo}$ , while the constant term vanishes:

$$\mathbf{f}_{buo} = -g \rho_f \int_B 1 \, dV = -g \underbrace{\rho_f \text{Vol}(B)}_{m_f :=}, \quad \mathbf{f}_{const} = \int_{\Omega} \nabla c \, dV = 0, \quad (14)$$

where  $m_f$  is the mass of the fluid displaced by the body's volume. The buoyant force exerts a torque through the center of volume  $\mathbf{c}_{vol} \in \mathbb{R}^3$ :

$$\tau_{buo} = - \int_B \mathbf{z} \times \rho_f \mathbf{g} \, dV_z = -\mathbf{c}_{vol} \times m_f \mathbf{g}. \quad (15)$$

To study the contribution of the dynamic pressure force  $\mathbf{f}_{dp}$  (Eq. 13), we need a more detailed discussion of the actual slip velocity  $\mathbf{u}_s$  experienced at the surface, detailed below.

#### 4.4 Flow separation estimation

We now come to one of our core contributions: a methodology for incorporating flow separation and surface slip velocity estimation. The formulation up until now assumes potential (laminar) flow, which is valid primarily at low Reynolds numbers. At moderate to high Reynolds numbers, *flow separation* typically arises along the surface, strongly affecting the surface slip velocity.

Flow separation highlights the fundamental difficulty of accurately predicting fluid forces for general geometries. As a result, shape-specific drag and lift coefficients  $C_D$  and  $C_L$ , typically parameterized by Reynolds number and angle of attack, have become standard in the literature (Sec. 2). These coefficients encapsulate pressure and friction effects implicitly and are commonly derived through heuristic or data-driven approaches, often calibrated via wind tunnel experiments where forces are decomposed relative to a fixed global *incoming flow direction*, a concept that does not transfer to bodies that also spin. Since accurately resolving this phenomenon is highly complex and incompatible with real-time performance, we propose the following simplifying assumptions:

- (1) When a point  $\mathbf{z} \in S$  moves away from the fluid (towards the body's interior) beyond a critical angular threshold  $\alpha$ , we assume that the fluid flow is detached from the surface at that point.
- (2) In regions of strong potential flow, partial viscous detachment is presumed to reduce the effective slip velocity and thereby the resulting dynamic pressure  $p_{dp}$ .
- (3) The induced wake is assumed to remain spatially confined and small relative to the characteristic length scale of the rigid body.

Assumption (1) introduces a criterion for flow separation based on local flow attachment, used to modify the potential surface slip velocity  $\mathbf{u}_s^\phi$ . Specifically, if a surface point  $\mathbf{z} \in S$  is moving away from the surrounding fluid beyond a critical angle, it is considered to lie within the separated wake region, effectively shielded from external flow. In such cases, we want our surface slip velocity to be zero (see Fig. 5d). This modification eliminates the dynamic pressure force  $\mathbf{f}_{dp}$  (Eq. (13)) contribution at surface points where the flow is detached.

Assumption (2) proposes a refinement of the potential surface slip velocity. The quantity  $\mathbf{u}_s^\phi$  represents the *ideal flow condition*, but its direct use tends to overestimate the resulting dynamic pressure  $p_{dyn}$ . A more physically plausible model accounts for viscous effects, which dampen tangential flow near the surface due to boundary layer effects. This reduction is particularly pronounced in regions where  $\nabla\phi$  exhibits strong tangential components.

To approximate this behavior, we propose to omit the tangential component  $\nabla\phi^\parallel$  when evaluating the surface slip velocity for dynamic pressure computation as a way to counter the overestimation and incorporate the effects of the fluid boundary layers. The normal component is given by the Neumann boundary condition as  $\nabla\phi^\perp = \langle \mathbf{v} + \mathbf{w} \times \mathbf{z}, \mathbf{n}_z \rangle \mathbf{n}_z$ . Thus, removing  $\nabla\phi^\parallel$  in the computation of  $\mathbf{u}_s^\phi$  is equivalent to projecting the velocity onto the tangent plane of the surface via the linear projection operator  $\mathcal{P}_{\mathbf{n}_z}$ :

$$\begin{aligned} \mathbf{u}_s^\phi - \nabla\phi^\parallel &= \nabla\phi^\perp - (\mathbf{v} + \mathbf{w} \times \mathbf{z}) \\ &= -(\mathbf{v} + \mathbf{w} \times \mathbf{z} - \langle \mathbf{v} + \mathbf{w} \times \mathbf{z}, \mathbf{n}_z \rangle \mathbf{n}_z) \\ &= -\underbrace{(\text{Id} - \mathbf{n}_z \cdot \mathbf{n}_z^\top)(\mathbf{v} + \mathbf{w} \times \mathbf{z})}_{\mathcal{P}_{\mathbf{n}_z}(\mathbf{z})} = \mathbf{U} \begin{bmatrix} \mathbf{w} \\ \mathbf{v} \end{bmatrix}. \end{aligned} \quad (16)$$

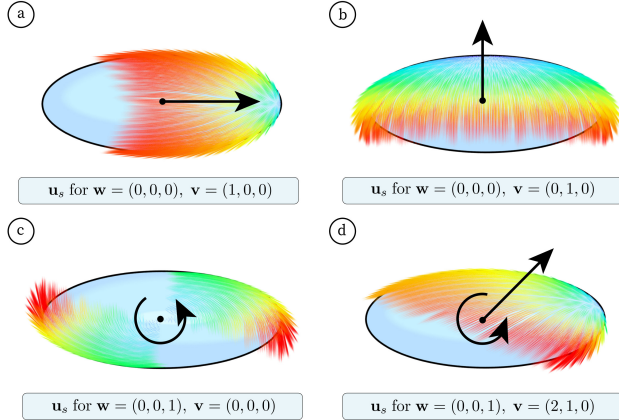


Fig. 6. Surface slip velocities  $\mathbf{u}_s$  (Eq. (16)) resulting from rigid body motion ( $\mathbf{w}, \mathbf{v}$ ) for an elliptical body (3D-view). (a) Horizontal velocity. (b) Vertical velocity. (c) Rotation induces antisymmetric slip velocities. (d) A linear combination of the previous velocities. Colors indicate velocity magnitude from blue (low) to red (high). Larger slip velocities induce a larger dynamic pressure on the surface.

Here,  $\mathbf{U}(\mathbf{z})$  is defined to be the linear operator mapping  $(\mathbf{w}, \mathbf{v})$  to  $\mathbf{u}_s^\phi - \nabla\phi\parallel$ . The modifications introduced by Assumptions (1) and (2) are encoded in the definition of the (non-potential) surface slip velocity:

$$\mathbf{u}_s(\mathbf{z}) := \begin{cases} \mathbf{U}(\mathbf{z}) \begin{bmatrix} \mathbf{w} \\ \mathbf{v} \end{bmatrix} & , \quad \langle \mathbf{n}_z, \frac{\mathbf{v} + \mathbf{w} \times \mathbf{z}}{\|\mathbf{v} + \mathbf{w} \times \mathbf{z}\|} \rangle < \cos \alpha, \\ 0 & , \text{ else.} \end{cases} \quad (17)$$

The *separation angle*  $\alpha \in [\frac{\pi}{2}, \pi]$  controls the flow detachment condition. Assumption (3) justifies that potential flow remains a valid approximation for global fluid behavior (Eq. (6)), thus enabling the use of surface integrals in Eq. (8) and the resulting fluid inertia  $\mathbf{K}_f$  as a sufficient estimate for the added mass. The slip velocity  $\mathbf{u}_s$  with separation angle  $\alpha = \frac{\pi}{2}$  is visualized in Fig. 6.

#### 4.5 Choice of separation angle $\alpha$

The occurrence of flow separation is often predicted by the Reynolds number  $Re \in \mathbb{R}$ , but only in a qualitative or empirical sense, and does not provide a predictive criterion to estimate the separation angle  $\alpha$ .  $Re$  is indifferent to sharp edges that strongly facilitate flow separation, or to surface roughness, which can delay the onset of separation (an effect that is well known in the case of dimpled golf balls, see Sec. 6.3).

Fortunately, the range of choices in our experience is very limited. In all of our experiments (Sec. 6) we denote the flow separation angle used by writing  $x\frac{\pi}{2} = \alpha \in [\frac{\pi}{2}, \pi]$  with  $x \in [1, 2]$ . The common default value is  $\alpha = \frac{\pi}{2}$ , and most deviations are related to surface roughness such as the golf ball in Sec. 6.3 where we use  $\alpha = 1.5\frac{\pi}{2}$ . Higher values of  $\alpha$  indicate stronger flow attachment.

#### 4.6 Skin-friction force

The roughness of the surface and the viscous interaction between the fluid and the solid boundary generate a tangential force that opposes the slip velocity  $\mathbf{u}_s$ . The friction force  $\mathbf{f}_{fr}$  and torque  $\tau_{fr}$  can be estimated via the idealized *Blasius solution* [Schlichting and Gersten 2017] for turbulent flow:

$$\begin{aligned} \mathbf{f}_{fr} &= \int_S -\frac{1}{2} C_f(\mathbf{z}) \rho_f \|\mathbf{u}_s(\mathbf{z})\| \mathbf{u}_s(\mathbf{z}) dA_z \\ \tau_{fr} &= \int_S \mathbf{z} \times \left( -\frac{1}{2} C_f(\mathbf{z}) \rho_f \|\mathbf{u}_s(\mathbf{z})\| \mathbf{u}_s(\mathbf{z}) \right) dA_z, \end{aligned} \quad (18)$$

with

$$C_f(\mathbf{z}) = 0.0576 \cdot Re_z^{-1/5}, \quad Re_z = \frac{\rho_f \|\mathbf{u}_s(\mathbf{z})\| L}{\mu}, \quad (19)$$

where we choose  $L = \sqrt{\text{total area}}$  as the characteristic length. The skin-friction  $\mathbf{f}_{fr}$  is typically orders of magnitude smaller than the dynamic pressure force  $\mathbf{f}_{dp}$  and only relevant in light, fast-moving objects such as a golf ball (Fig. 11).

### 5 Discretization and simulation

We now implement the computations described in Sec. 4. The rigid body  $B$  is discretized as a triangular surface mesh with vertices and faces ( $V, F$ ). Each face  $f_i \in F$  is associated with a barycenter  $\mathbf{c}_i \in \mathbb{R}^3$ , a unit normal  $\mathbf{n}_i \in \mathbb{R}^3$ , and an area  $A_i > 0$ . The total mass of the body and the displaced fluid are denoted by  $m_b$  and  $m_f$ , respectively.

#### 5.1 Potential flow solving

As established in Sec. 4.1, there exists a linear mapping  $\mathbf{P}_\phi$  from rigid body velocities  $(\mathbf{w}, \mathbf{v})$  to the associated potential field  $\phi$  (Eq. (7)). We discretize  $\phi$  using continuous piecewise linear hat functions centered at mesh vertices  $v_i$ , yielding a  $\#V \times 6$  matrix representation of  $\mathbf{P}_\phi$ .

To ensure comparability and ease of implementation, we solve for the values of  $\phi_i$  at the vertices using the common *potential source point method*, as done in [Weißmann and Pinkall 2012b]. Solving the Neumann-boundary problem for the  $j$ th component of  $(\mathbf{w}, \mathbf{v})$  yields the  $j$ th column of the matrix  $\mathbf{P}_\phi$  (Eq. (7)).

#### 5.2 Computing the inertia

For  $\mathbf{K}_b$ : If the body is considered to have uniform density  $\rho_b$ , then we compute the body inertia tensor  $\mathbf{K}_b$  according to [Kallay 2006]. Otherwise, we prescribe masses  $m_i \in \mathbb{R}_+$  to the barycenters of faces and compute the inertia in the classical point-based way.

For  $\mathbf{K}_f$ : Due to the linear hat function representation of the potential  $\phi$ , we can exactly realize the  $6 \times \#V$  matrix  $\mathbf{M}_\phi : (\mathbf{w}, \mathbf{v}) \mapsto (\mathbf{I}, \mathbf{p})$  (see Appendix A.1). The fluid inertia is then computed by the matrix multiplication  $\mathbf{K}_f = \mathbf{M}_\phi \mathbf{P}_\phi$  (Eq. (9)).

#### 5.3 Force and torque evaluations

The surface slip velocity  $\mathbf{u}_s$ , as computed by the local normal projection  $\mathcal{P}_{\mathbf{n}_z}$  (Eq. (16)), is linear with respect to the rigid body velocities  $(\mathbf{w}, \mathbf{v})$ . Thus, we can construct a matrix  $\mathbf{U} \in \mathbb{R}^{3 \times \#F \times 6}$  that maps  $(\mathbf{w}, \mathbf{v})$  directly to each face's slip velocities  $\mathbf{u}_{s,i} = \mathbf{u}_s(\mathbf{c}_i) \in \mathbb{R}^3$  at the face centers (Appendix A.2). We then apply our flow separation estimation on  $\mathbf{u}_{s,i}$  (Eq. (17)) to compute the discrete dynamic pressure

force and torque using the equations:

$$\begin{aligned} \mathbf{f}_{dp} &= \sum_{i=1}^{\#F} -\frac{1}{2} \rho_f \|\mathbf{u}_{s,i}\|^2 A_i \mathbf{n}_i, \\ \tau_{dp} &= \sum_{i=1}^{\#F} \mathbf{c}_i \times \left( -\frac{1}{2} \rho_f \|\mathbf{u}_{s,i}\|^2 A_i \mathbf{n}_i \right). \end{aligned} \quad (20)$$

To compute the gravitational and buoyant forces  $\mathbf{f}_g, \mathbf{f}_{buo}$  we transform the world-frame gravity vector  $\mathbf{g}_w$  to the body-frame  $\mathbf{g} = \mathbf{q}^{-1} \mathbf{g}_w \mathbf{q}$ . The gravitational force  $\mathbf{f}_g$  acts on the center of mass  $\mathbf{c}_m$  (origin in body-frame) and therefore has vanishing torque  $\tau_g$ . The buoyant force  $\mathbf{f}_{buo}$  acts on the center of volume  $\mathbf{c}_{vol}$  and thus exerts a torque. We combine gravity and buoyancy into the following equations:

$$\mathbf{f}_{gb} := (m_b - m_f) \mathbf{g}, \quad \tau_{gb} := -\mathbf{c}_{vol} \times m_f \mathbf{g}. \quad (21)$$

The skin-friction force and torque are computed similarly by

$$\begin{aligned} \mathbf{f}_{fr} &= \sum_{i=1}^{\#F} -\frac{1}{2} C_f(\mathbf{c}_i) \rho_f \|\mathbf{u}_{s,i}\| A_i \mathbf{u}_{s,i}, \\ \tau_{fr} &= \sum_{i=1}^{\#F} \mathbf{c}_i \times \left( -\frac{1}{2} C_f(\mathbf{c}_i) \rho_f \|\mathbf{u}_{s,i}\| A_i \mathbf{u}_{s,i} \right). \end{aligned} \quad (22)$$

The gyroscopic force terms ( $\tau_{gyro}, \mathbf{f}_{gyro}$ ) of Eq. (4) are treated like any other force (Alg. 2).

#### 5.4 Algorithm and integration

Prior to simulation, we perform a preprocessing step for each rigid body to compute the combined body-fluid inertia tensor  $\mathbf{K} \in \mathbb{R}^{6 \times 6}$  (Sec. 5.2) and the slip velocity matrix  $\mathbf{U} \in \mathbb{R}^{3\#F \times 6}$  (Appendix A.2).

Given the equations of motion (Eq. (4)) and the force models described here, our method supports integration using any conventional time-stepping scheme. In practice, a symplectic Euler integrator with Lie group updates for the quaternion  $\mathbf{q}$  is sufficient in most scenarios. For cases involving large angular velocities  $\mathbf{w}$ , we adopt a fourth-order Runge–Kutta integrator with adaptive substepping to maintain stability by maintaining  $\|\mathbf{w}\| \Delta t < 5.7^\circ$ .

By precomputing the fluid inertia and formulating all fluid interactions as additional forces within the RBD framework, our approach enables accurate real-time simulation of body–fluid interactions without full fluid simulation or heuristic lift/drag coefficients. This design allows seamless integration with existing RBD solvers and generalizes across shapes. In the following section we demonstrate that this minimal setup suffices to reproduce intricate fluid phenomena such as falling plate modes, the Magnus effect, the tight spiral pass of a football and others. The core structure of our implementation is summarized in Algorithms 1 and 2.

## 6 Results

We implement our rigid body dynamics solver in Python and evaluate its performance across a range of fluid–body interaction scenarios. These experiments are designed to assess the fidelity, generality and robustness of the proposed model. Corresponding simulation videos for all scenarios are provided in the supplementary material. *A complete executable implementation will be provided upon publication.*

---

#### Algorithm 1: PREPROCESSING

---

**Input:** Triangle mesh  $(V, F)$ , initial state  $(\mathbf{q}, \mathbf{y}, \mathbf{w}, \mathbf{v})$ , body mass  $m_b$ , fluid density  $\rho_f$ , timestep  $\Delta t$   
**Output:** Updated states  $(\mathbf{q}, \mathbf{y}, \mathbf{w}, \mathbf{v})$  over time

1 **Preprocessing (once per mesh):**  
2 Compute  $\mathbf{K}$  // Inertia (Sec. 4.2)  
3 Compute  $\mathbf{U}$  // Slip velocity (App. A.2)

4 **Time integration loop: while simulation is running do**  
5  $\mathbf{q}, \mathbf{y}, \mathbf{w}, \mathbf{v} \leftarrow \text{INTEGRATE}(\mathbf{q}, \mathbf{y}, \mathbf{w}, \mathbf{v}, \Delta t)$  //

---

#### Algorithm 2: INTEGRATE

---

**Input:** State  $(\mathbf{q}, \mathbf{y}, \mathbf{v}, \mathbf{w})$ , timestep  $\Delta t$   
**Data:** Inertia  $\mathbf{K}$ , slip velocity matrix  $\mathbf{U}$ , separation angle  $\alpha$ .  
**Output:** Updated state  $(\mathbf{q}', \mathbf{y}', \mathbf{v}', \mathbf{w}')$

1  $\begin{bmatrix} 1 \\ \mathbf{p} \end{bmatrix} \leftarrow \mathbf{K} \begin{bmatrix} \mathbf{w} \\ \mathbf{v} \end{bmatrix}$  // Eq. (1)  
2  $\mathbf{u}_s \leftarrow \mathbf{U} \begin{bmatrix} \mathbf{w} \\ \mathbf{v} \end{bmatrix}$  // Eq. (16)  
3  $\mathbf{u}_s \leftarrow \text{FLOWSEPARATIONESTIMATION}(\mathbf{u}_s, \alpha)$  // Eq. (17)  
4  $\begin{bmatrix} \tau_{dp} \\ \mathbf{f}_{dp} \end{bmatrix} \leftarrow \text{DYNAMICPRESSUREFORCE}(\mathbf{u}_s)$  // Eq. (20)  
5  $\begin{bmatrix} \tau_{gyro} \\ \mathbf{f}_{gyro} \end{bmatrix} \leftarrow \begin{bmatrix} \mathbf{l} \times \mathbf{w} + \mathbf{p} \times \mathbf{v} \\ \mathbf{p} \times \mathbf{w} \end{bmatrix}$  // Eq. (4)  
6  $\begin{bmatrix} \tau_{gb} \\ \mathbf{f}_{gb} \end{bmatrix} \leftarrow \begin{bmatrix} -\mathbf{c}_{vol} \times m_f \mathbf{g} \\ (m_b - m_f) \mathbf{g} \end{bmatrix}$  // Eq. (21)  
7  $\begin{bmatrix} \tau_{fr} \\ \mathbf{f}_{fr} \end{bmatrix} \leftarrow \text{SKINFRICTIONFORCE}(\mathbf{u}_s)$  // Eq. (22)  
8  $\begin{bmatrix} \mathbf{f} \\ \mathbf{l} \end{bmatrix} \leftarrow \begin{bmatrix} \tau_{gyro} + \tau_{gb} + \tau_{dp} + \tau_{fr} \\ \mathbf{f}_{gyro} + \mathbf{f}_{gb} + \mathbf{f}_{dp} + \mathbf{f}_{fr} \end{bmatrix}$  // Eq. (4)  
9  $\begin{bmatrix} \mathbf{l}' \\ \mathbf{p}' \end{bmatrix} = \text{INTEGRATE}(\mathbf{l}, \mathbf{p}, \mathbf{f}, \Delta t)$  // Eq. (4)  
10  $\begin{bmatrix} \mathbf{w}' \\ \mathbf{v}' \end{bmatrix} \leftarrow \mathbf{K}^{-1} \begin{bmatrix} \mathbf{l}' \\ \mathbf{p}' \end{bmatrix}$  // Eq. (1)  
11  $\begin{bmatrix} \mathbf{q}' \\ \mathbf{y}' \end{bmatrix} = \text{INTEGRATE}(\mathbf{q}, \mathbf{y}, \dot{\mathbf{q}}, \dot{\mathbf{y}}, \Delta t)$  // Eq. (4)  
12 **return**  $(\mathbf{q}', \mathbf{y}', \mathbf{v}', \mathbf{w}')$

---

All simulation parameters are physically determined from the respective experimental setups, with the exception of the flow separation angle  $\alpha$  (Eq. (17)), which is fixed at  $\frac{\pi}{2}$  unless otherwise specified. The fluid density  $\rho_f$  is set to that of air ( $1.204 \text{ kg/m}^3$ ) or water ( $998 \text{ kg/m}^3$ ), depending on the scenario.

As discussed in Section 6.9, the fluid interaction phenomena studied in our experiments involve inherently unstable and complex dynamics, which preclude the availability of quantifiable ground-truth data. Full fluid simulations are not suitable as a reference, since they introduce strong dependencies on the chosen numerical method and parameterization. We therefore follow the validation strategy established in prior work on rigid body dynamics in ambient fluids, focusing on reproducing known phenomena and directly comparing our results to theirs.

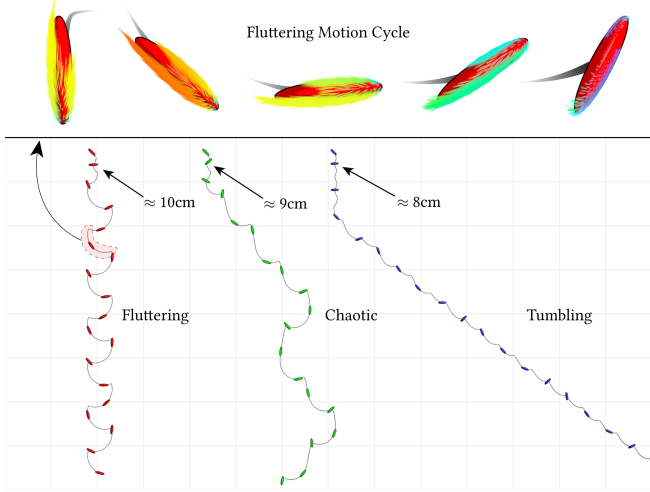


Fig. 7. Characteristic falling plate dynamics reproduced by our method through small variations in the width of an elliptical body. **Bottom left:** *Fluttering* mode, showing periodic lateral oscillations. **Bottom middle:** *Chaotic* descent, marked by irregular transitions between fluttering and tumbling. **Bottom right:** *Tumbling* motion, characterized by continuous overturning. **Top:** Close-up of a fluttering cycle with surface slip velocity  $u_s$  visualized using infrared-style coloring, where red indicates high slip speed and blue indicates low slip speed.

### 6.1 Falling thin plates

As described in Sec. 2, reproducing the unsteady dynamics of falling plates has historically relied on full fluid simulations or the use of specialized solvers. In our formulation, we model falling thin plates as light, axisymmetric ellipses with a width-to-height ratio of 5:1. Following the observations of Andersen et al. [2005], the resulting falling behavior is primarily governed by the plate's inertia. We fix the mass at 0.2 g and vary the width of the plate from 8 cm to 10 cm to control the moment of inertia. Our model successfully captures the characteristic falling regimes: *fluttering* (a periodic lateral swaying motion) for a 10 cm ellipse, *tumbling* (continuous overturning) for an 8 cm ellipse and the intermediate *chaotic* mode (an aperiodic transition between fluttering and tumbling) for a 9 cm ellipse. We use  $\alpha = \frac{\pi}{2}$ .

Fig. 8 illustrates the transition in the falling dynamics of thin plates as a function of mass. At low mass, pronounced fluid–body coupling induces large-amplitude fluttering trajectories. With increasing mass, the motion stabilizes into an expected stable vertical descent [Lau et al. 2018]. In the heavy-mass regime, fluid interactions becomes negligible and the trajectory converges to a free-fall motion consistent with classical rigid body dynamics.

### 6.2 The Magnus effect

Spinning bodies experience lateral aerodynamic forces, causing a trajectory deflection known as the Magnus effect [Anderson 2010]. We conduct three experiments that depend on this effect.

*Curved shot of a soccer ball.* The Magnus effect is used for *curled shots*, where imparted spin causes the ball to follow a curved path.

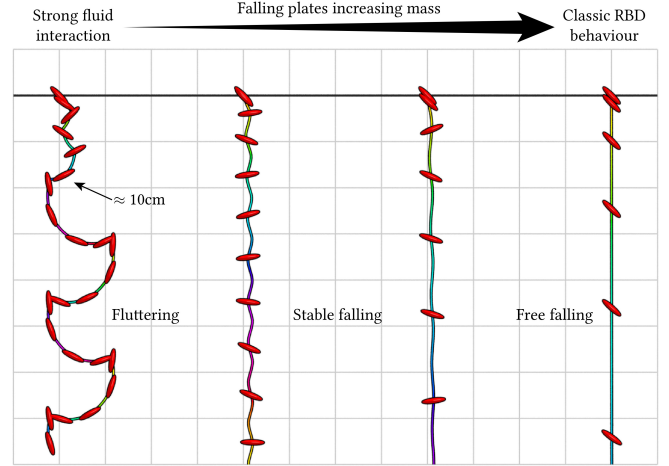


Fig. 8. Falling plate trajectories for increasing mass. Light plates exhibit pronounced fluttering due to strong fluid interaction. As the mass increases, the motion transitions to stable falling (flat side tends downwards) and eventually to free fall (like in vacuum), converging toward classical rigid-body dynamics. The path color indicates elapsed time through a hue cycle.

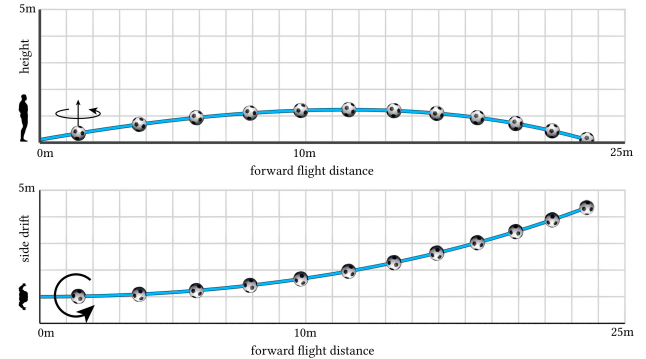


Fig. 9. Simulation of a spinning soccer ball exhibiting side drift due to the Magnus effect. Parameters approximate the 1997 Roberto Carlos free kick. The ball size is exaggerated for visual clarity.

Our model naturally reproduces this effect through the relative pressure difference on each side of the spinning object. We reproduce the iconic 1997 Roberto Carlos free kick using only estimates [Asal 1998] of the velocity ( $\approx 30$  m/s), spin ( $\approx 10$  rps), as well as the common size and weight of a soccer ball and achieve the expected 4m lateral drift (Fig. 1, 9).

*Basketball drop.* When a spinning basketball is dropped from a significant height, the Magnus effect induces a substantial forward drift. Using standard parameters for basketball size and mass, our model reproduces this behavior (Fig. 10) in agreement with video footage [2015]. Due to the basketball's rougher surface compared to a soccer ball, flow separation is delayed, which we capture by adjusting the critical separation angle to  $\alpha = 1.2\frac{\pi}{2}$ .

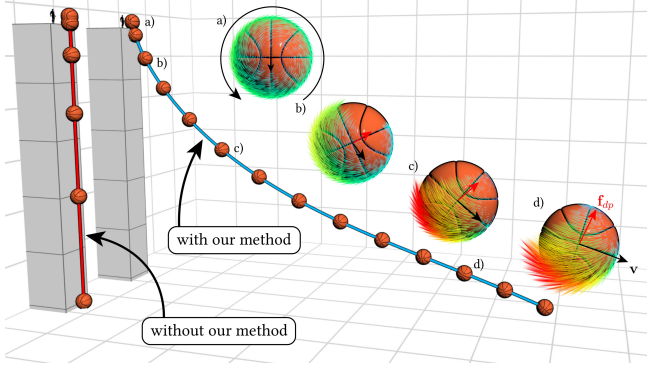


Fig. 10. Magnus-induced forward drift of a spinning basketball dropped from a height. The delayed onset of flow separation due to surface roughness is modeled by increasing the separation angle  $\alpha = 1.2\frac{\pi}{2}$ , which effectively extends the region of attached flow and enhances lateral lift through the resulting dynamic pressure force  $f_{dp}$ . We also show the spinning basketball trajectory using classical rigid body dynamics on the left. The ball sizes are exaggerated for visual clarity.

### 6.3 Golf ball flight

Golf balls exhibit significant aerodynamic effects arising from their surface geometry and spin. Dimples on the surface induce earlier boundary layer transition, delaying flow separation and shifting the separation point downstream, which effectively reduces pressure drag [Choi et al. 2006]. In our model, this effect is represented by increasing the flow separation angle to  $\alpha = 1.5\frac{\pi}{2}$ .

We simulate the launch of a 45 g golf ball using the parameters specified by the *Overall Distance Standard* [2023a], which include a launch velocity of approximately 53 m/s, a launch angle of 10°, and a backspin rate of 42 rps. This configuration predicts a horizontal flight distance of approximately 289 m. Fig. 11 illustrates the resulting trajectories for balls with and without dimples, as well as with and without backspin. The presence of dimples increases the effective flight range by reducing drag, while backspin generates additional lift via the Magnus effect. The simulated trajectory reaches a horizontal distance of 290 m, consistent with the standard. At this relatively low launch angle, both dimples and backspin play a crucial role in sustaining lift and extending flight duration. Notably, this is the only example in this work in which the skin-friction force  $f_{fr}$  (Sec. 4.6) accumulates to become non-negligible.

### 6.4 Tight spiral pass

A well-thrown American football spins rapidly around its symmetry axis, yet during flight, this axis turns to follow the curved trajectory, despite the football being symmetric in the forward-backward direction, torque-free and evenly weighted. This long-standing puzzle, known as the *tight spiral paradox*, was resolved only recently [Price et al. 2020], showing that subtle aerodynamic torques cause a precession aligning the nose with the velocity vector.

We simulate a typical throw: 27.4 m/s, 10 rad/s, 30° angle,  $\approx 66.4$  m range,  $\approx 2.8$  s flight duration [Rae 2003], and estimate  $\alpha = 1.5\frac{\pi}{2}$  because of the rough surface and low curvature in the direction of travel reducing flow separation. When throwing the ball at an initial

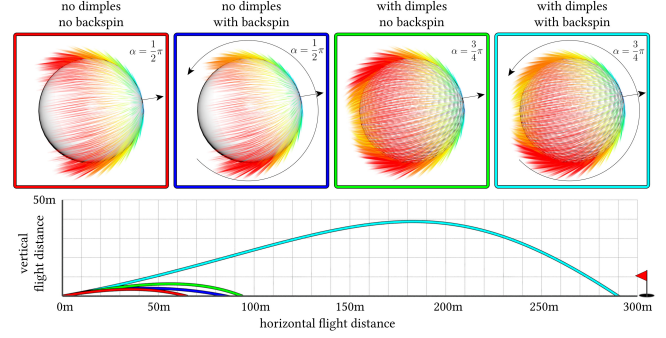


Fig. 11. A golf ball is shot at launch angle of 10°, with 53 m/s. The dimples on the ball delay the flow separation, which we model by increasing the separation angle  $\alpha = 1.5\frac{\pi}{2}$ . Further adding a backspin (42 rps) increases the flight distance through the Magnus effect, yielding realistic flight distances as specified by the *Overall Distance Standard* [2023b]. Red: a golf ball without dimples or backspin. Green: without dimples and with backspin. Blue: with dimples and without backspin. Cyan: with dimples and backspin. Top: the surface slip velocities  $u_s$  are shown with infrared coloring from blue (low speed) to red (high speed). Bottom: the flight trajectories in a graph. Notice how the backspin causes asymmetric slip velocities and thus a stronger pressure force at the bottom of the golf ball.

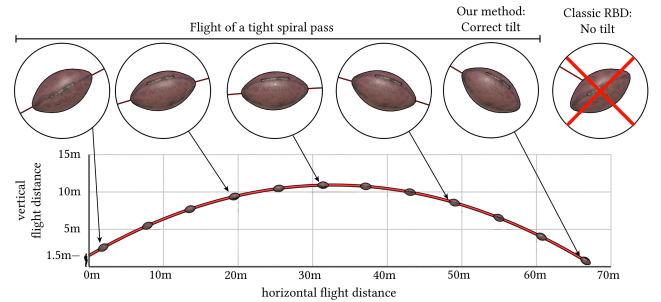


Fig. 12. Simulated American football throw. Our model reproduces the correct alignment of the spin axis with the trajectory, capturing the subtle aerodynamic effects responsible for the *tight spiral paradox* [Price et al. 2020]. The ball size is exaggerated for visual clarity.

height of 1.5 m, we recover the correct precessional alignment of the spin axis with the trajectory (Fig. 12), and the ball touches the ground at approximately 67.6 m after 2.85 s. In the absence of our introduced fluid effects, the football's spin axis does not align with its trajectory (Fig. 12).

### 6.5 Underwater motion

Simulating underwater dynamics in our model requires only adjusting the fluid density to that of water ( $\rho_f = 998 \text{ kg/m}^3$ ), enabling direct comparison with the experimental results of Weißmann and Pinkall [2012b]. We also reproduce the observed dynamics from their recordings by estimating the size and mass of the objects used in their experiments (Fig. 13), without the need to adjust any unphysical parameters.

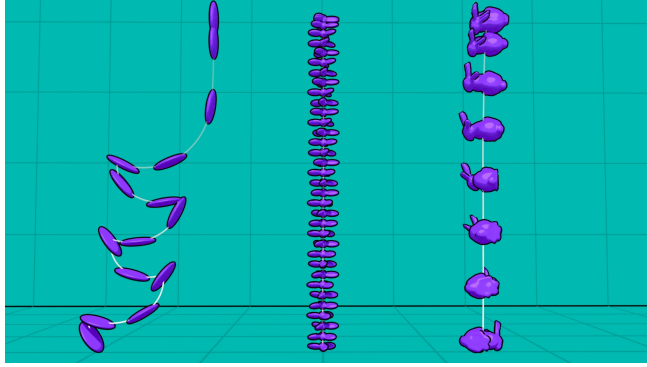


Fig. 13. A silicone ( $\rho_b = 1060 \text{ kg/m}^3$ ) ellipsoid, a propeller, and a bunny are released underwater, reproducing the experimental footage available in [Weißmann and Pinkall 2012b].

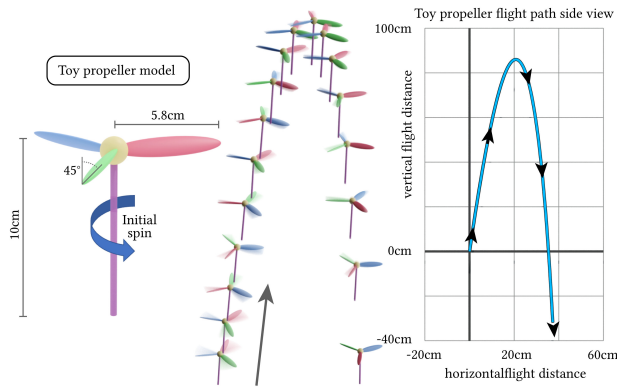


Fig. 14. Ascent of a spinning toy propeller reproduced by our model via aerodynamic lift generated from a high initial angular momentum. The propeller starts slightly tilted with zero linear momentum  $p$  and takes off by converting angular momentum into linear momentum due to the fluid interaction.

## 6.6 Spinning toy propeller

When rapidly spun and released, lightweight propeller toys convert rotational motion into lift through aerodynamic interactions. Our model reproduces this ascent behavior without requiring any additional modifications, as shown in Fig. 14. We tilt the propeller slightly to achieve a curved flight path. We use  $\alpha = \frac{\pi}{2}$ .

## 6.7 Buoyant dynamics of balloons

Balloons exhibit highly unsteady motion due to the large torque induced by the offset between their center of mass and center of volume. This buoyant torque leads to pronounced rotational instability even under small perturbations. Our model accurately captures this behavior ( $\alpha = \frac{\pi}{2}$ ), consistent with the experimental footage in [Weißmann and Pinkall 2012b].

## 6.8 Spinning paper copter

To further demonstrate the generality of our approach, we simulate the free fall of a light paper copter. The offset mass distribution and

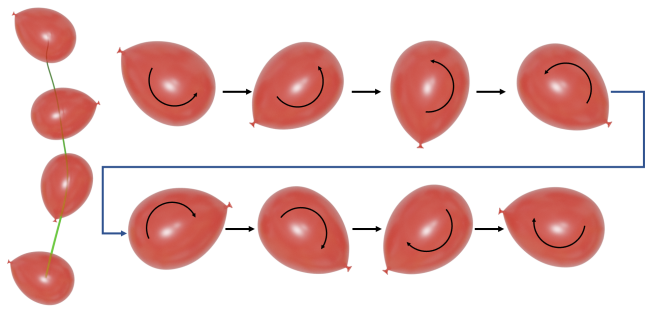


Fig. 15. Simulated buoyant motion of an air balloon. The offset between center of mass and center of volume induces a destabilizing torque, leading to unsteady, realistic dynamics. The balloon is initially at rest.

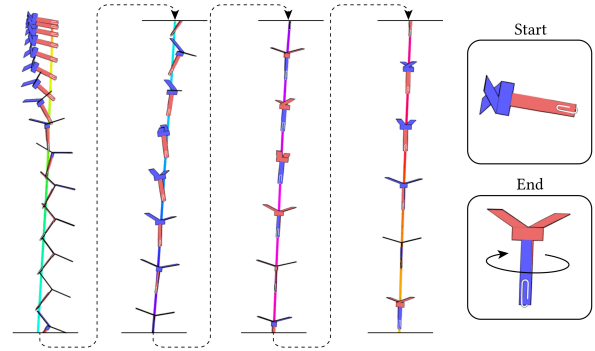


Fig. 16. Simulation of a freely falling paper copter exhibiting autorotation. The offset mass distribution induces a restoring torque that aligns the copter with its descent direction, leading to stable autorotation.

dynamic pressure drag generate a restoring torque that passively aligns the copter's axis with the direction of descent. This alignment promotes autorotation, stabilizing the fall through the surrounding fluid (Fig. 16,  $\alpha = \frac{\pi}{2}$ ). We regard this example as a limitation, as the thin structure had to be replaced with a slightly wider proxy geometry due to the difficulty of solving the Neumann boundary problem at thin edges (Sec. 6.11).

## 6.9 Comparison with existing work

We evaluate our algorithm in direct comparison with the two most closely related approaches that address rigid body dynamics in ambient fluids and explicitly incorporate the fluid inertia tensor in the equations of motion. Following the validation strategy established in earlier work, we focus on reproducing known phenomena and include classical rigid body dynamics as a baseline reference.

*Under water rigid body dynamics (UWRBD)* [Weißmann and Pinkall 2012b]. The UWRBD work employs the same computation for the inertia tensor  $\mathbf{K}_f$  as we do, but introduces an additional scaling factor  $\lambda$  to artificially *balance angular and linear inertia*. While this can improve certain outcomes, the factor has no physical basis (we set

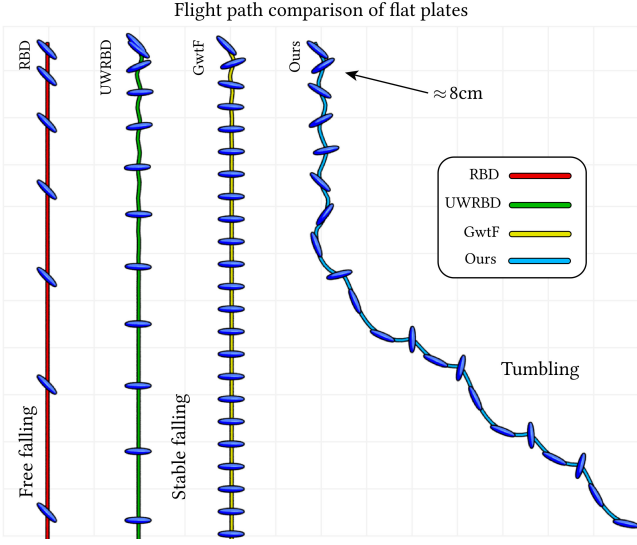


Fig. 17. Comparison of falling plates (8 cm diameter). Both UWRBD [Weißenmann and Pinkall 2012b] and GwtF [Soliman et al. 2024] overdampen the lateral motion, leading to unrealistically stable descent. When UWRBD (using  $\lambda = 1$ ) is given a lower linear drag coefficient, the simulation becomes unstable. Our method reproduces the experimentally observed tumbling mode.

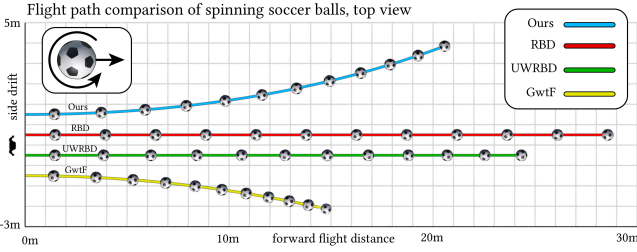


Fig. 18. Soccer ball trajectories with identical initial velocity and spin. UWRBD [Weißenmann and Pinkall 2012b] neglects lift and produces a nearly straight path with mild drag. GwtF [Soliman et al. 2024] introduces a drift opposite to the Magnus effect. Only our method reproduces the correct lateral deflection.

$\lambda = 1$ ). The method further relies on a linear drag model with a free parameter that controls stability.

*Going with the flow (GwtF)[Soliman et al. 2024].* GwtF approximates the inertia tensor with a formulation that is efficient to compute but valid only for convex shapes. Their force formulation combines lift and drag into a compact per-face rule. Although their primary goal is to analyze the momentum evolution of deforming shapes, applying their model to a fixed geometry yields a rigid body dynamics simulation.

For consistency, all comparisons employ the same inertia tensor evaluation and identical numerical integration (RK4). This ensures that differences arise only from the respective fluid force formulations. Figures 17, 18, 19 and 20 illustrate the resulting behaviors across representative experiments.

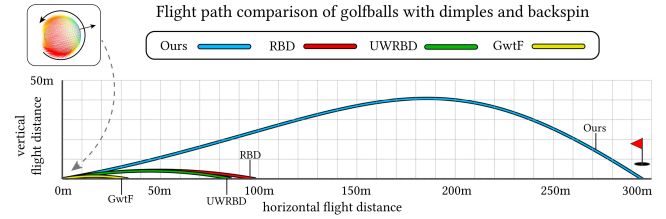


Fig. 19. Backspinning dimpled golf ball trajectories. UWRBD [Weißenmann and Pinkall 2012b] and GwtF [Soliman et al. 2024] further shorten the flight relative to rigid body dynamics. Our method recovers the expected increase in range due to backspin [USGA 2023b].

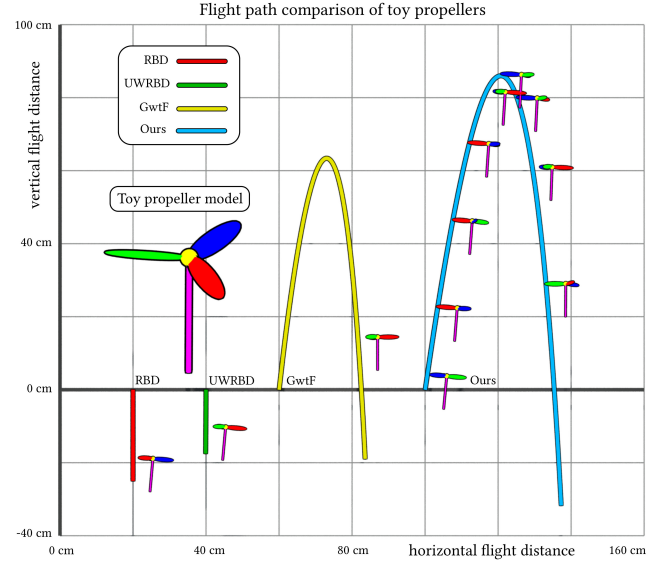


Fig. 20. Toy propeller launches with identical initial spin and release angle. UWRBD [Weißenmann and Pinkall 2012b] yields slightly slower descent than rigid body dynamics, while both GwtF [Soliman et al. 2024] and our method capture the expected lift-induced flight path, although at different scales.

Overall, UWRBD lacks any lift forces and suffers from its linear drag formulation: small parameter choices lead to instabilities, while large values can overdampen the results. They focus on underwater settings to mitigate these problems. GwtF includes both lift and drag, producing more stable trajectories, but their choice of forces overdampens the system and suppresses key aerodynamic effects; in particular, their model fails to reproduce the Magnus-effect drift in the correct direction. In contrast, our formulation derives lift and drag implicitly from surface pressures, yielding stable simulations that capture the correct dynamic behaviors without artificial damping.

## 6.10 Performance

All experiments are conducted on an i9-14900KF CPU. Performance results are summarized in Table 2.

*Preprocessing.* The fluid inertia tensor  $K_f$  is computed by solving six boundary integral equations (BIEs), each involving the same

dense  $\#V \times \#V$  linear system. This  $O(\#V^3)$  step constitutes the primary computational bottleneck, but is executed only once per mesh. Preprocessing times are reported in Table 2.

*Simulation loop.* During simulation, each timestep involves a force evaluation and a single RBD integrator step. The equations of motion operate on six-dimensional state vectors, with the exception of the dynamic pressure force, which requires a parallelizable per-face sum. The per-step timings scale linearly with  $\#F$  and are also shown in Table 2. We report baseline RBD runtimes to quantify the overhead factor introduced by our model.

### 6.11 Limitations and future work

Limitations of our method primarily stem from the piecewise linear hat function discretization used to represent the surface potential  $\phi$ . While effective for most geometries, this choice can under-resolve flow features near sharp edges or thin wings where the potential varies strongly. Additionally, the BIE-based preprocessing requires a dense matrix solve, making it impractical for very high-resolution meshes. In practice, we recommend using simplified proxy meshes and note that fast multipole methods or higher-order basis functions may offer future improvements for more efficient BIE solves.

Although the  $\alpha$  parameter has a clear physical interpretation and does not vary substantially, we leave it to future work to estimate this parameter directly from the body’s shape, roughness and/or current Reynolds number, which we have not yet been able to connect. Furthermore, our current formulation of the surface slip velocity in Eq. (11) could be refined to better capture subtle flow effects. Addressing these limitations would likely improve the accuracy of our framework and could possibly extend to include stable gliding and autorotation of winged seeds which we failed to reproduce.

## 7 Conclusion

We presented a minimal yet physically grounded extension to rigid body dynamics that captures complex fluid–body interactions without relying on full fluid simulations or heuristic lift and drag coefficients. By estimating dynamic surface pressure from potential flow and slip velocity, our method remains free from non-physical parameters and requires only the choice of a flow separation angle  $\alpha$ . Our work is the first to reproduce the full spectrum of falling thin plate modes—fluttering, tumbling and chaotic descent—using such a lightweight setup. This phenomenon has previously been assumed to require either full Navier–Stokes simulations or specialized solvers. Our results suggest that many complex effects, often attributed to detailed vortex dynamics, can be recovered through surface pressure asymmetries alone.

The outcome of this work is a robust and efficient framework that significantly enhances the realism of RBD simulations, which can be integrated into existing RBD solvers at only a modest computational cost. Additionally, the proposed methodology offers a promising foundation for advancing the modeling and understanding of rigid body–fluid interactions.

## Acknowledgments

This work was supported in part by the Alexander von Humboldt Foundation through a Feodor Lynen Research Fellowship and the

European Research Council (ERC) under the European Union’s Horizon 2020 research and innovation program (grant agreement No. 101003104, ERC CoG MYCLOTH). Additional support was provided by SideFX software.

## References

Nadir Akinci, Markus Ihmsen, Gizem Akinci, Barbara Solenthaler, and Matthias Teschner. 2012. Versatile rigid-fluid coupling for incompressible SPH. *ACM Trans. Graph.* 31, 4 (2012), 62:1–62:8. doi:10.1145/2185520.2185558

A. Andersen, U. Pesavento, and Z. Jane Wang. 2005. Unsteady aerodynamics of fluttering and tumbling plates. *Journal of Fluid Mechanics* 541 (2005), 65–90. doi:10.1017/S002211200500594X

John D. Anderson. 2010. *Fundamentals of Aerodynamics*. McGraw-Hill Education. Google-Books-ID: xw8PgAACAJ.

Alexis Angelidis and Fabrice Neyret. 2005. Simulation of smoke based on vortex filament primitives. In *Proceedings of the 2005 ACM SIGGRAPH/Eurographics symposium on Computer animation* (New York, NY, USA, 2005-07-29) (SCA ’05). Association for Computing Machinery, 87–96. doi:10.1145/1073368.1073380

Takeshi Asai. 1998. *The physics of football*. <https://physicsworld.com/a/the-physics-of-football/>

J. W. Banks, W. D. Henshaw, D. W. Schwendeman, and Qi Tang. 2017. A stable partitioned FSI algorithm for rigid bodies and incompressible flow. Part II: General formulation. *J. Comput. Phys.* 343 (2017), 469–500. doi:10.1016/j.jcp.2017.04.064

David Baraff. 1997. An Introduction to Physically Based Modeling: Rigid Body Simulation I–III. Published: SIGGRAPH ’97 Course Notes, Course 30.

Markus Becker, Hendrik Tessendorf, and Matthias Teschner. 2009. Direct Forcing for Lagrangian Rigid-Fluid Coupling. *IEEE Transactions on Visualization and Computer Graphics* 15, 3 (2009), 493–503. doi:10.1109/TVCG.2008.107

Mark Carlson, Peter J. Mucha, and Greg Turk. 2004. Rigid fluid: animating the interplay between rigid bodies and fluid. *ACM Trans. Graph.* 23, 3 (2004), 377–384. doi:10.1145/1015706.1015733

Qiang Chen, Zhiqiang Deng, Feng Li, Yuming Fang, Tingsong Lu, Yang Tong, and Yifan Zuo. 2024. Real-time Wing Deformation Simulations for Flying Insects. In *ACM SIGGRAPH 2024 Conference Papers* (New York, NY, USA, 2024-07-13) (SIGGRAPH ’24). Association for Computing Machinery, 1–11. doi:10.1145/3641519.3657434

Jin Choi, Woo-Pyung Jeon, and Haecheon Choi. 2006. Mechanism of drag reduction by dimples on a sphere. *Physics of Fluids* 18, 4 (2006), 041702. doi:10.1063/1.2191848

Herbert Goldstein, Charles Poole, and John Safko. 2002. *Classical Mechanics* (3rd ed.). Addison Wesley.

Oliver Gross, Yousuf Soliman, Marcel Padilla, Felix Knöppel, Ulrich Pinkall, and Peter Schröder. 2023. Motion from Shape Change. *ACM Trans. Graph.* 42, 4 (2023), 107:1–107:11. doi:10.1145/3592417

How Ridiculous. 2015. What Happens When a Spinning Basketball is Thrown Off a Dam! [https://www.youtube.com/watch?v=QtP\\_bh2lMXc](https://www.youtube.com/watch?v=QtP_bh2lMXc)

Wentao Huang, Hong Liu, Fuxin Wang, Junqi Wu, and H. P. Zhang. 2013. Experimental study of a freely falling plate with an inhomogeneous mass distribution. *Physical Review E* 88, 5 (2013), 053008. doi:10.1103/PhysRevE.88.053008 Publisher: American Physical Society.

Michael Kallay. 2006. Computing the Moment of Inertia of a Solid Defined by a Triangle Mesh. *Journal of Graphics Tools* 11, 2 (2006), 51–57. doi:10.1080/2151237X.2006.10129220 Publisher: Taylor & Francis \_eprint: <https://doi.org/10.1080/2151237X.2006.10129220>

G. R. Kirchhoff. 1870. On the Motion of a Solid of Revolution in a Fluid. *Journal für die Reine und Angewandte Mathematik* 71 (1870).

L. D. Landau and E. M. Lifshitz. 1976. *Mechanics* (3rd ed.). Course of Theoretical Physics, Vol. 1. Pergamon Press.

David Lannes. 2017. On the Dynamics of Floating Structures. *Annals of PDE* 3, 1 (2017), 11. doi:10.1007/s40818-017-0029-5

Edwin M. Lau, Wei-Xi Huang, and Chun-Xiao Xu. 2018. Progression of heavy plates from stable falling to tumbling flight. *Journal of Fluid Mechanics* 850 (2018), 1009–1031. doi:10.1017/jfm.2018.486

Qiqin Le, Jiamu Bu, Yanke Qu, Bo Zhu, and Tao Du. 2024. Computational Biomimetics of Winged Seeds. *ACM Trans. Graph.* 43, 6 (2024), 180:1–180:13. doi:10.1145/3687899

Zhehao Li, Qingyu Xu, Xiaohan Ye, Bo Ren, and Ligang Liu. 2023. DiffFFR: Differentiable SPH-Based Fluid–Rigid Coupling for Rigid Body Control. *ACM Trans. Graph.* 42, 6 (2023), 179:1–179:17. doi:10.1145/3618318

Maxwell. 1890. On a particular case of the descent of a heavy body in a resisting medium. In *The Scientific Papers of James Clerk Maxwell*, W. D. Niven (Ed.). Cambridge Library Collection - Physical Sciences, Vol. 1. Cambridge University Press, 115–118. doi:10.1017/CBO9780511698095.008

Sehee Min, Jungdam Won, Seunghwan Lee, Jungnam Park, and Jehee Lee. 2019. SoftCon: simulation and control of soft-bodied animals with biomimetic actuators. *ACM Trans. Graph.* 38, 6 (2019), 208:1–208:12. doi:10.1145/3355089.3356497

Table 2. Computation times for preprocessing and simulation loop steps of our algorithm when run on a i9-14900KF CPU for all our experiments. We also report the baseline RBD runtime (without fluid interaction), the relative computational overhead, and relevant parameters. Fast-spinning objects require significantly more substeps to remain stable.

Experiment Figure	plate Fig.7	soccer Fig.9	basket Fig.10	golf Fig.11	golf spin Fig.11	football Fig.12	bunny Fig.13	toy Fig.14	balloon Fig.15	paper Fig.16
Vertices $\#V \in \mathbb{N}$	450	252	252	252	252	392	468	526	252	1347
Faces $\#F \in \mathbb{N}$	896	500	500	500	500	780	932	1048	500	2690
Separation angle $\alpha \in [\frac{\pi}{2}, \pi]$	$\frac{\pi}{2}$	$\frac{\pi}{2}$	$1.2 \frac{\pi}{2}$	$\frac{\pi}{2}, 1.5 \frac{\pi}{2}$	$\frac{\pi}{2}, 1.5 \frac{\pi}{2}$	$1.5 \frac{\pi}{2}$	$1.1 \frac{\pi}{2}$	$\frac{\pi}{2}$	$\frac{\pi}{2}$	$\frac{\pi}{2}$
Preprocessing time (ms)	532.1	92.86	93.5	96.03	93.01	352.02	588.98	1.15 s	111.4	5.08 s
Step time (ms)	2.58	30.22	42.97	2.05	79.07	47.98	2.73	129.75	2.02	5.44
Step time classic RBD (ms)	0.51	5.85	8.47	0.59	15.9	7.89	0.56	17.19	0.56	0.59
Overhead factor	$\times 5.07$	$\times 5.16$	$\times 5.07$	$\times 3.49$	$\times 4.97$	$\times 6.08$	$\times 4.91$	$\times 7.55$	$\times 3.59$	$\times 9.25$
Time step (s)	0.03	0.03	0.03	0.02	0.02	0.03	0.03	0.03	0.03	0.01
Max num. substeps	1	17	24	1	44	21	1	50	1	1

Isaac Newton. 1687. *Newton's Principia : the mathematical principles of natural philosophy*. New-York : Published by Daniel Adee. <http://archive.org/details/newtonspmathema00newtrich>

Oktar Ozgen, Marcela Kallmann, Lynnette Es Ramirez, and Carlos Fm Coimbra. 2010. Underwater cloth simulation with fractional derivatives. *ACM Trans. Graph.* 29, 3 (2010), 23:1–23:9. doi:10.1145/1805964.1805967

Marcel Padilla, Albert Chern, Felix Knöppel, Ulrich Pinkall, and Peter Schröder. 2019. On bubble rings and ink chandeliers. *ACM Trans. Graph.* 38, 4 (2019), 129:1–129:14. doi:10.1145/3306346.3322962

Umberto Pesavento and Z. Jane Wang. 2004. Falling Paper: Navier-Stokes Solutions, Model of Fluid Forces, and Center of Mass Elevation. *Physical Review Letters* 93, 14 (2004), 144501. doi:10.1103/PhysRevLett.93.144501 Publisher: American Physical Society.

Richard H. Price, William C. Moss, and T. J. Gay. 2020. The paradox of the tight spiral pass in American football: A simple resolution. *American Journal of Physics* 88, 9 (2020), 704–710. doi:10.1119/10.0001388

T. Probst and M. Teschner. 2023. Monolithic Friction and Contact Handling for Rigid Bodies and Fluids Using SPH. *Computer Graphics Forum* 42, 1 (2023), 155–179. doi:10.1111/cgf.14727 \_eprint: <https://onlinelibrary.wiley.com/doi/pdf/10.1111/cgf.14727>

William J. Rae. 2003. Flight dynamics of an American football in a forward pass. *Sports Engineering* 6, 3 (2003), 149–163. doi:10.1007/BF02859892

A. Rana, V. K. Kushwaha, and Arnab Kumar De. 2020. A numerical study on the effect of aspect-ratio and density ratio on the dynamics of freely falling plate in the flutter-to-tumble transition regime. *Sādhanā* 45, 1 (2020), 259. doi:10.1007/s12046-020-01487-y

J. Roenby, S. Aliyar, and H. Bredmose. 2024. A robust algorithm for computational floating body dynamics. *Royal Society Open Science* 11, 4 (2024), 231453. doi:10.1098/rsos.231453 Publisher: Royal Society.

Hermann Schlichting and Klaus Gersten. 2017. *Boundary-Layer Theory*. Springer. doi:10.1007/978-3-662-52919-5

Sung-Ik Sohn. 2024. Simulation of the unsteady vortical flow of freely falling plates. *Theoretical and Computational Fluid Dynamics* 38, 6 (2024), 779–799. doi:10.1007/s00162-024-00686-1

Yousuf Soliman, Marcel Padilla, Oliver Gross, Felix Knöppel, Ulrich Pinkall, and Peter Schröder. 2024. Going with the Flow. *ACM Trans. Graph.* 43, 4 (2024), 57:1–57:12. doi:10.1145/3658164

Adrien Treuille, Andrew Lewis, and Zoran Popović. 2006. Model reduction for real-time fluids. *ACM Trans. Graph.* 25, 3 (2006), 826–834. doi:10.1145/1141911.1141962

Xiaoyuan Tu and Demetri Terzopoulos. 1994. Artificial fishes: physics, locomotion, perception, behavior. In *Proceedings of the 21st annual conference on Computer graphics and interactive techniques* (New York, NY, USA, 1994-07-24) (SIGGRAPH '94). Association for Computing Machinery, 43–50. doi:10.1145/192161.192170

Nobuyuki Umetani, Yuki Koyama, Ryan Schmidt, and Takeo Igarashi. 2014. Pteromys: interactive design and optimization of free-formed free-flight model airplanes. *ACM Trans. Graph.* 33, 4 (2014), 65:1–65:10. doi:10.1145/2601097.2601129

USGA. 2023a. *The Golf Ball and Distance: Frequently Asked Questions*. <https://www.usga.org/content/usga/home-page/advancing-the-game/distance-insights/golf-ball-revised-testing-guidelines-frequently-asked-questions.html>

USGA. 2023b. *The Golf Ball and Distance: Frequently Asked Questions*. <https://www.usga.org/content/usga/home-page/advancing-the-game/distance-insights/golf-ball-revised-testing-guidelines-frequently-asked-questions.html> Authority: USGA.

Steffen Weißmann and Ulrich Pinkall. 2010a. Filament-based smoke with vortex shedding and variational reconnection. In *ACM SIGGRAPH 2010 Papers* (New York, NY, USA, 2010) (SIGGRAPH '10). Association for Computing Machinery. doi:10.1145/1833349.1778852 event-place: Los Angeles, California.

Steffen Weißmann and Ulrich Pinkall. 2012b. Underwater rigid body dynamics. *ACM Trans. Graph.* 31, 4 (2012), 104:1–104:7. doi:10.1145/2185520.2185600

Jakub Wejchert and David Haumann. 1991. Animation aerodynamics. *SIGGRAPH Comput. Graph.* 25, 4 (1991), 19–22. doi:10.1145/127719.122719

Jia-chi Wu and Zoran Popović. 2003. Realistic modeling of bird flight animations. *ACM Trans. Graph.* 22, 3 (2003), 888–895. doi:10.1145/882262.882360

R.-J. Wu and S.-Y. Lin. 2015. The Flow of A Falling Ellipse: Numerical Method and Classification. *Journal of Mechanics* 31, 6 (2015), 771–782. doi:10.1017/jmech.2015.47

Yang Xiang, Suyang Qin, Wentao Huang, Fuxin Wang, and Hong Liu. 2018. Trajectory modes and wake patterns of freely falling plates. *Journal of Visualization* 21, 3 (2018), 433–441. doi:10.1007/s12650-017-0469-8

Hongjiu Zhong, Shiyi Chen, and Cunbiao Lee. 2011. Experimental study of freely falling thin disks: Transition from planar zigzag to spiral. *Physics of Fluids* 23, 1 (2011), 011702. doi:10.1063/1.3541844

## A Detailed calculations

We discretize the surface potential  $\phi$  using continuous, piecewise linear basis functions  $h_i$ , each defined to take the value 1 at vertex  $z_i$  and 0 at all other mesh vertices:

$$\phi(\mathbf{z}) = \sum_{i=1}^{\#V} \phi_i h_i(\mathbf{z}). \quad (23)$$

In the discrete setting, we treat  $\phi$  as an element of  $\mathbb{R}^{\#V}$ . The surface  $S$  is discretized as a union of triangular faces  $f \in F$  with constant normals  $\mathbf{n}_i \in \mathbb{R}^3$  during integration. For each vertex  $v_i$ , we denote by  $N_{f,i}$  the set of incident faces sharing that vertex.

### A.1 From potential $\phi$ to momenta $(\mathbf{l}, \mathbf{p})$

Given a potential field  $\phi$  represented in terms of vertex-based linear hat functions  $h_i$ , we construct the matrix operator  $\mathbf{M}_\phi \in \mathbb{R}^{6 \times \#V}$  that maps scalar potential to the corresponding fluid-induced angular and linear momenta  $(\mathbf{l}_f, \mathbf{p}_f)$ , as defined in Eq. (8). Substituting the

expansion  $\phi(\mathbf{z}) = \sum_i \phi_i h_i(\mathbf{z})$  into the momentum integrals yields:

$$\begin{aligned} \mathbf{l}_f &= \rho_f \int_S \phi(\mathbf{z}) \mathbf{z} \times \mathbf{n} \, dA_{\mathbf{z}} = \sum_{i=1}^{\#V} \underbrace{\left( \rho_f \int_S h_i(\mathbf{z}) \mathbf{z} \times \mathbf{n} \, dA_{\mathbf{z}} \right)}_{\mathbf{l}_{f,i} :=} \phi_i, \\ \mathbf{p}_f &= \rho_f \int_S \phi(\mathbf{z}) \mathbf{n} \, dA_{\mathbf{z}} = \sum_{i=1}^{\#V} \underbrace{\left( \rho_f \int_S h_i(\mathbf{z}) \mathbf{n} \, dA_{\mathbf{z}} \right)}_{\mathbf{p}_{f,i} :=} \phi_i. \end{aligned} \quad (24)$$

The quantities  $\mathbf{l}_{f,i}$  and  $\mathbf{p}_{f,i}$  admit further simplification by exploiting the local support of  $h_i$ , which is nonzero only on the faces incident to vertex  $v_i$ :

$$\begin{aligned} \mathbf{l}_{f,i} &= \sum_{f_j \in N_{f,i}} \rho_f \int_{f_j} h_i(\mathbf{z}) \mathbf{z} \, dA_{\mathbf{z}} \times \mathbf{n}_j \\ &= \sum_{f_j \in N_{f,i}} \frac{1}{12} \rho_f A_j (2\mathbf{z}_{j,i_0} + \mathbf{z}_{j,i_1} + \mathbf{z}_{j,i_2}) \times \mathbf{n}_j, \\ \mathbf{p}_{f,i} &= \sum_{f_j \in N_{f,i}} \rho_f \int_{f_j} h_i(\mathbf{z}) \, dA_{\mathbf{z}} \mathbf{n}_j = \sum_{f_j \in N_{f,i}} \frac{1}{3} \rho_f A_j \mathbf{n}_j, \end{aligned} \quad (25)$$

where the indices  $(i_0, i_1, i_2)$  denote the local ordering of vertices on face  $f_j$  with  $\mathbf{z}_{j,i_0} = \mathbf{z}_i$ . The matrix  $\mathbf{M}_\phi$  is then constructed by

stacking the row vectors  $\mathbf{l}_{f,i}$  and  $\mathbf{p}_{f,i}$  into a single  $6 \times \#V$  matrix:

$$\mathbf{M}_\phi = \begin{bmatrix} \mathbf{l}_{f,1} & \cdots & \mathbf{l}_{f,\#V} \\ \mathbf{p}_{f,1} & \cdots & \mathbf{p}_{f,\#V} \end{bmatrix}. \quad (26)$$

## A.2 Slip velocity matrix

We now discretize the linear operator  $\mathbf{U}$  that maps rigid body velocities  $(\mathbf{w}, \mathbf{v})$  to the corresponding slip velocities  $\mathbf{u}_{s,i}$  at the barycenters  $\mathbf{c}_i$  of each triangle face  $f_i \in F$ . To this end, we define a matrix  $\mathbf{R} \in \mathbb{R}^{3\#F \times 6}$  that maps the body velocities  $(\mathbf{w}, \mathbf{v})$  to the rigid body surface velocity evaluated at the face centers, i.e.,  $\mathbf{v} + \mathbf{w} \times \mathbf{c}_i$ . For each face  $f_i$ , the local mapping is given by:

$$\mathbf{v} + \mathbf{w} \times \mathbf{c}_i = \underbrace{\begin{bmatrix} -[\mathbf{c}_i \times] & \text{Id} \end{bmatrix}}_{=: \mathbf{R}_i} \begin{bmatrix} \mathbf{w} \\ \mathbf{v} \end{bmatrix}, \quad (27)$$

where  $[\mathbf{c}_i \times]$  denotes the  $3 \times 3$  skew-symmetric matrix representing the cross product with  $\mathbf{c}_i$ . The full matrix  $\mathbf{R}$  is obtained by stacking the row blocks  $\mathbf{R}_i \in \mathbb{R}^{3 \times 6}$  for all  $f_i \in F$ .

The slip velocity matrix  $\mathbf{U}$  is the negative normal projection operator  $\mathcal{P}_{\mathbf{n}_z}$  applied to the rigid body surface velocity output of  $\mathbf{R}$  (Eq. (16)):

$$\mathbf{U} = - \begin{bmatrix} \mathcal{P}_{\mathbf{n}_{\mathbf{c}_1}} \mathbf{R}_1 \\ \vdots \\ \mathcal{P}_{\mathbf{n}_{\mathbf{c}_{\#F}}} \mathbf{R}_{\#F} \end{bmatrix} \in \mathbb{R}^{3\#F \times 6}. \quad (28)$$

Received TBD 2025; revised TBD 2025; accepted TBD 2025